


 Cite this: *RSC Adv.*, 2023, **13**, 3333

Electrical transport properties of $\text{TiO}_2/\text{MAPbI}_3$ and $\text{SnO}_2/\text{MAPbI}_3$ heterojunction interfaces under high pressure†

Yuqiang Li, ^{*ad} Yuhong Li, ^{ad} Qiang Zhang, ^b Xiaofeng Liu, ^c Yuanjing Li, ^{ad} Ningru Xiao, ^e Pingfan Ning, ^d Jingjing Wang, ^{ad} Jianxin Zhang^{ad} and Hongwei Liu^{ad}

The electrical transport properties of $\text{SnO}_2(\text{TiO}_2)/\text{MAPbI}_3$ (MA = CH_3NH_3^+) heterojunction interfaces are investigated from ambient pressure to 20 GPa, and the transport properties are calculated by physical parameters such as trap energy density, binding energy, and charge transfer driving force and defect. Based on the partial density of states (PDOS) of the $\text{SnO}_2/\text{MAPbI}_3$ heterojunction interface MA-termination and PbI_2 -termination, greater charge transfer driving force and higher binding energy are observed, obviously showing the SnO_2 -based heterojunction is more stable. The $\text{SnO}_2/\text{MAPbI}_3$ heterojunction interface possesses stronger electrical transport ability and is less prone to capture electrons compared with the $\text{TiO}_2/\text{MAPbI}_3$ heterojunction interface. The differential charge density spectrum shows that the density is lower in the trap energy level of $\text{SnO}_2/\text{MAPbI}_3$, whilst the effect of the charge transfer defect is weaker owing to the trap energy level only existing in SnO_2 . The $\text{SnO}_2/\text{MAPbI}_3$ heterostructure interface is less prone to capture electrons. The greater electron concentration difference is attributed to oxygen vacancy (V_{O_0}) in the SnO -like environment, resulting in superior electron transport ability compared with the TiO -like environment.

Received 21st December 2022
 Accepted 3rd January 2023

DOI: 10.1039/d2ra08143a
rsc.li/rsc-advances

1. Introduction

In the field of PSCs (perovskite solar cells), the interface problem is one of the key factors to determine efficiency and stability.^{1–3} MAPbI_3 thin films can form heterojunction interfaces with TiO_2 or SnO_2 , which will cause lattice distortion in the interface, affect electrical transport properties, and accelerate ion migration.^{4–6} TiO_2 and SnO_2 respectively form electrical transport complexes $\text{O}_2\text{-Ti}^{4+}$ and $\text{O}_2\text{-Sn}^{4+}$.^{7,8} SnO_2 is considered a substitute for TiO_2 due to its high electron mobility,⁹ transmittance, and stability,^{10–12} and less IV hysteresis. However, the band matching of $\text{SnO}_2/\text{MAPbI}_3$ is worse than that of $\text{TiO}_2/\text{MAPbI}_3$.^{13,14} Generally, the comparative analysis of PSC efficiency for the $\text{SnO}_2/\text{MAPbI}_3$ and $\text{TiO}_2/\text{MAPbI}_3$ electron transport layers is complex.

Leijtens *et al.*¹⁵ reported that oxygen adsorption instability acted on the electrical transport characteristics of the $\text{TiO}_2/\text{MAPbI}_3$ heterojunction surface under the excitation of ultraviolet light, because the holes on the valence band of TiO_2 recombine with the electrons at the oxygen adsorption point, resulting in the release of adsorbed oxygen molecules, forming a free electron and a positively charged oxygen vacancy on the conduction band. Yang *et al.*¹⁶ reported a method of drastically improving solar cell efficiency by surface optimization of the TiO_2 electron transport layer (ETL) using a special ionic-liquid (IL), which shows high optical transparency and superior electron mobility. Shin *et al.*¹⁷ found a low-temperature colloidal method for depositing La-doped BaSnO_3 films as a replacement for TiO_2 to reduce ultraviolet-induced damage, and the solar cells retained over 90% of their initial performance after 1000 hours of full sun illumination. Giordano *et al.*¹⁸ demonstrated that Li-doped TiO_2 electrodes exhibit superior electronic properties, by reducing electronic trap states enabling faster electron transport. Guo *et al.*¹⁹ proposed that a $\text{SnO}_2:\text{InCl}_3$ ETL was used in planar PSCs to simultaneously dope the ETL and passivate the defects at the ETL/perovskite interface, which expands the ETL/perovskite interface optimization work by using anions and cations for passivation and doping, respectively. Park²⁰ demonstrated that trap density in the MAPbI_3 close to TiO_2 was far lower than that without TiO_2 , evidenced by the gate voltage-dependent threshold voltage difference based on the field effect transistor (FET) structure. Kim *et al.*²¹ elucidated the atomistic

^aTianjin Key Laboratory of Optoelectronic Detection Technology and Systems, School of Electronic and Information Engineering, Tiangong University, Tianjin 300387, China.
 E-mail: liyuqiang@tiangong.edu.cn

^bKey Laboratory of Smart Grid of Ministry of Education, School of Electrical and Information Engineering, Tianjin University, Tianjin 300072, China

^cTianjin San'an Optoelectronics Co., LTD, Tianjin 300384, China

^dEngineering Research Center of High Power Solid State Lighting Application System of Ministry of Education, Tiangong University, Tianjin 300387, China

^eSchool of Physical Science and Technology, Tiangong University, Tianjin 300387, China

† Electronic supplementary information (ESI) available. See DOI: <https://doi.org/10.1039/d2ra08143a>



origin of efficient electron extraction and long stability of SnO_2 based PSCs through the analysis of band alignment, carrier injection, and interfacial defects in the $\text{SnO}_2/\text{MAPbI}_3$ interface using first-principles calculations at the Perdew–Burke–Ernzerhof (PBE0) + spin–orbit-coupling (SOC) + Tkatchenko–Scheffler (TS) dispersion-correction (PBE0-SOC-TS) level for all possible terminations and MA directions.

So far, most of the studies have focused on the enhancement of the electron mobility of $\text{SnO}_2(\text{TiO}_2)/\text{MAPbI}_3$ heterojunction interfaces by passivation and doping under ambient conditions and the interface oxygen vacancy induced by temperature and light. The electrical transport characteristics of $\text{SnO}_2(\text{TiO}_2)/\text{MAPbI}_3$ heterojunction interfaces under high pressure are rarely studied. High pressure has been proven to be a clean and powerful tool to analyze the physical properties of various heterojunction interfaces.^{22,23} In this article, the electrical transport properties of $\text{SnO}_2(\text{TiO}_2)/\text{MAPbI}_3$ heterojunction interfaces are investigated from ambient to 20 GPa pressure by theoretical calculations, and the transport properties are investigated using physical parameters such as trap energy density, binding energy, charge transfer driving force and defects, and charge-capture rate. The electron transport abilities of $\text{SnO}_2(\text{TiO}_2)/\text{MAPbI}_3$ heterojunction interfaces are compared through the driving force of charge transfer, trap level density, and charge transfer defects calculations, using PDOS and differential charge density spectra under different pressures up to 20 GPa.

2. Theoretical basis and methods

We perform the noncollinear density functional theory (DFT) calculations with the hybrid PBE0 functional²⁴ including TS dispersion correction²⁵ using the Vienna *Ab initio* Simulation Package (VASP)²⁶ with dipole corrections. This is because the PBE0 functional can describe the band alignment of our system very well. In order to choose suitable exchange–correlations, we complete band gap calculation for SnO_2 , TiO_2 , and MAPbI_3 with different exchange–correlations using the PBE0-SOC-TS. We note that regardless of the exchange–correlation, the theoretical band gap is larger in TiO_2 , whereas the experimental band gap is larger in SnO_2 .²¹ Therefore, instead of choosing different exchange–correlations for the $\text{SnO}_2/\text{MAPbI}_3$ and $\text{TiO}_2/\text{MAPbI}_3$ interfaces, we select only one potential for the whole interface calculations which can minimize the average band gap error. Since the PBE0-SOC-TS gives the minimum band gap error compared with the experimental band gap, we choose the PBE0-SOC-TS exchange–correlation. We uncover the mechanism behind the superior SnO_2 –(TiO_2)-based PSCs by employing first-principles calculations using the PBE0-SOC-TS level for the $\text{SnO}_2(\text{TiO}_2)/\text{MAPbI}_3$ interface system owing to the lowest average band gap error. The projection augmented wave (PAW) method is used to carry out relevant calculations, using the Kohn–Sham (KS) equation based on density functional theory DFT,^{27,28} a comparative study is performed on the ETL of SnO_2 /

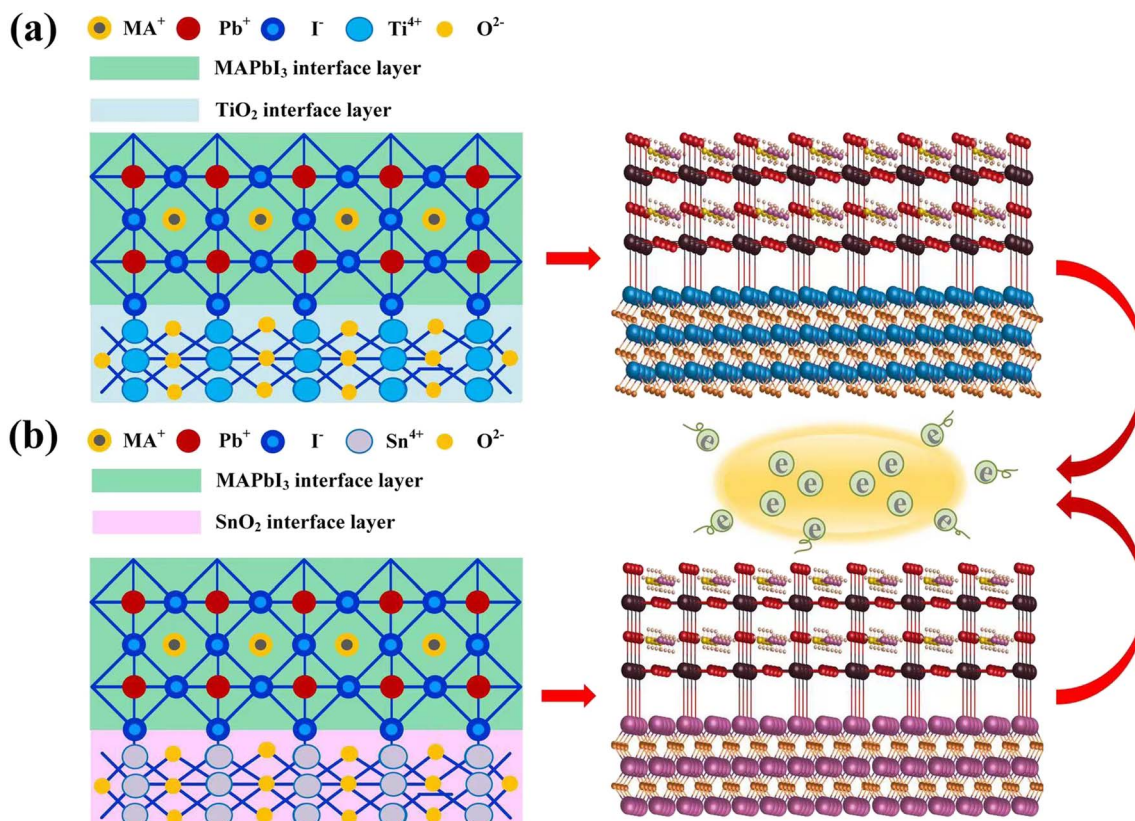


Fig. 1 Optimized models and structures of (a) $\text{TiO}_2/\text{MAPbI}_3$ heterojunction interface, (b) $\text{SnO}_2/\text{MAPbI}_3$ heterojunction interface, showing electron-capture mechanism similarly.



MAPbI₃ and TiO₂/MAPbI₃ heterojunction interfaces. Using the optimized SnO₂(TiO₂)/MAPbI₃ heterojunction interface modules, energy band, PDOS, and differential charge density spectrum are calculated from ambient pressure to 20 GPa.

Corresponding to the homologous electron-capture mechanism, the optimized models of the TiO₂/MAPbI₃ and SnO₂/MAPbI₃ heterojunction interfaces are shown in Fig. 1(a) and (b), respectively. The parameters of SnO₂(TiO₂)/MAPbI₃ heterojunction interface models are set (Table S3 in ESI†). The crystal cells on the surfaces of the [001], [011] and [111] plane SnO₂ and TiO₂, and [001] plane cubic MAPbI₃ are studied at 0 GPa, 5 GPa, 10 GPa, and 15 GPa. The slab consists of symmetric SnO₂ or TiO₂ (5 layers, 22 Sn/Ti atoms, and 44 O atoms) and MAPbI₃ [001], [011] and [111] (3 layers; MAI-termination: 4 MA molecules, 3 Pb atoms, and 10 I atoms; PbI₂-termination: 3 MA molecules, 4 Pb atoms, and 11 I atoms), where the lattice mismatches of SnO₂(TiO₂)/MAPbI₃ heterojunction interface models are as small as $\sim 2.75\%$ with a vacuum size of ~ 40 Å. Atomic coordinates of $\sqrt{2} \times \sqrt{2}$ supercells of SnO₂(TiO₂)/MAPbI₃ heterojunction interface models are shown in Tables S1 and S2 in the ESI.† Considering the lattice parameters of pristine SnO₂ ($\sqrt{2} \times \sqrt{2}$ supercell) and MAPbI₃ ($\sqrt{2} \times \sqrt{2}$ supercell) are about 6.55 and 6.25 Å, respectively, the average lattice parameter of 6.4 Å is selected which makes the lattice mismatch of both sides 2.75%. With combinations of MAI- and PbI₂-terminations with [001], [011], and [111] directions of MA in MAPbI₃, six types of SnO₂/MAPbI₃ (Fig. S2(a)–(c) in the ESI†) and TiO₂/MAPbI₃ (Fig. S2(d)–(f) in the ESI†) heterojunction interfaces are investigated under high pressure up to 20 GPa. Using the GCA-PBE functional, the truncation energy is set to 500 eV and the sampling density at point K is set to $3 \times 3 \times 5$. The convergence

standard of structural optimization is that the difference in energy iteration is less than 1×10^{-6} eV per atom, the maximum force of atom is less than 0.02 eV Å⁻¹, and DFT+U is set. To reduce the lattice mismatch between MAPbI₃ and TiO₂ or SnO₂ in the DFT calculations, the initial distance between the four layers of atoms in the outermost layer of MAPbI₃ and TiO₂ or SnO₂ is set to 3.05 Å, and the vacuum layer at the heterojunction interface is set to 10.05 Å. Using the optimized TiO₂/MAPbI₃ and SnO₂/MAPbI₃ heterojunction interface models, the optimized Pb–I bond is relaxed from the original 3.15 Å to 3.45 Å, the length of the Ti–I bond and Sn–I bond is 3.38 Å, and the Pb–O bond is 2.35 Å. The area of the SnO₂(TiO₂)/MAPbI₃ heterojunction interface is selected to be about 1.68 nm². The optimized SnO₂/MAPbI₃ heterojunction interface shows stronger interface bonding and interface atom interaction.

3. Results and discussion

For the optimized SnO₂(TiO₂)/MAPbI₃ heterojunction interface modules, the interface binding energy of the two heterojunction interface models is:

$$\Delta E(\text{SnO}_2(\text{TiO}_2)/\text{MAPbI}_3) = E(\text{TiO}_2)/E(\text{SnO}_2) + E(\text{MAPbI}_3) - E(\text{SnO}_2(\text{TiO}_2)/\text{MAPbI}_3) \quad (1)$$

At the same time, the interface binding energy per unit area is:

$$\Delta E_{\text{unit}}(\text{SnO}_2(\text{TiO}_2)/\text{MAPbI}_3) = \frac{\Delta E(\text{SnO}_2(\text{TiO}_2)/\text{MAPbI}_3)}{S} \quad (2)$$

where $E(\text{SnO}_2)$, $E(\text{TiO}_2)$, and $E(\text{MAPbI}_3)$ respectively represent the energy of the SnO₂(TiO₂) and MAPbI₃ part before building

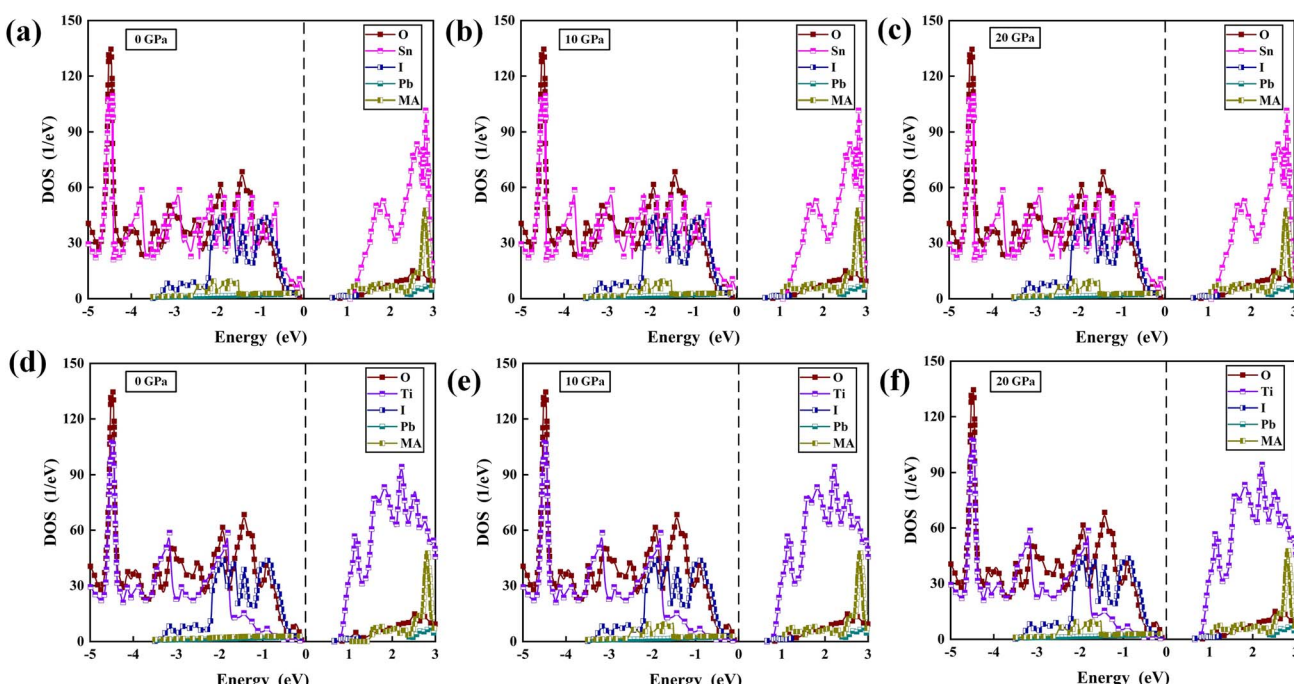


Fig. 2 PDOS of MA, Pb, I, Sn, O at (a) 0 GPa, (b) 10 GPa, (c) 20 GPa, and MA, Pb, I, Ti, O at (d) 0 GPa, (e) 10 GPa, (f) 20 GPa. Set Fermi energy level at 0 eV.



the $\text{SnO}_2(\text{TiO}_2)/\text{MAPbI}_3$ heterojunction interface models, $E(\text{SnO}_2(\text{TiO}_2)/\text{MAPbI}_3)$ represents the overall energy of the $\text{SnO}_2(\text{TiO}_2)/\text{MAPbI}_3$ heterojunction interface models, and S represents that the selected interface area is about 1.68 nm^2 . By comparing the binding energy values, we can quantify the relative stability of $\text{TiO}_2/\text{MAPbI}_3$ and $\text{SnO}_2/\text{MAPbI}_3$ heterojunction interface structures.

The MAPbI_3 model and $\text{SnO}_2(\text{TiO}_2)$ models of $\text{SnO}_2(\text{TiO}_2)/\text{MAPbI}_3$ heterojunction interfaces are optimized and calculated by static-self consistent calculations, and van der Waals force is introduced to correct them. The binding energy of $\text{SnO}_2/\text{MAPbI}_3$ [$\Delta E_{\text{unit}}(\text{SnO}_2/\text{MAPbI}_3) = -1.02 \text{ eV nm}^{-2}$] is significantly higher than the binding energy of $\text{TiO}_2/\text{MAPbI}_3$ [$\Delta E_{\text{unit}}(\text{TiO}_2/\text{MAPbI}_3) = -6.75 \text{ eV nm}^{-2}$] under ambient conditions (Table S4 in ESI†), which shows that the structure of the $\text{SnO}_2/\text{MAPbI}_3$ heterojunction interface is more stable. The $\text{SnO}_2/\text{MAPbI}_3$ heterojunction interface has higher interface binding energy, showing

stronger interface atom interactions and more stable heterojunction interface structure. The difference in binding energy is smaller with applied pressure up to 20 GPa since the binding energy of the $\text{SnO}_2/\text{MAPbI}_3$ heterojunction interface increases less (Table S5 in ESI†). Compared with the $\text{TiO}_2/\text{MAPbI}_3$ heterojunction interface, the larger interfacial binding energy of the $\text{SnO}_2/\text{MAPbI}_3$ heterojunction interface roughly keeps the stable Pb-I bond leading to improvement in electrical transport properties.^{29–31}

The PDOS of MA, Pb, I, Ti, Sn, and O in the $\text{TiO}_2/\text{MAPbI}_3$ and $\text{SnO}_2/\text{MAPbI}_3$ heterojunction interfaces are shown in Fig. 2(a)–(f) under different pressures, respectively. For the $\text{TiO}_2/\text{MAPbI}_3$ heterojunction interface, the Fermi level is at the top of the valence band and the width of the band gap is about 0.75 eV. The bottom CBM (Conduction Band Minimum) of the conduction band of TiO_2 is basically composed of the valence electrons of Ti atoms, and the bottom CBM of MAPbI_3 is mainly

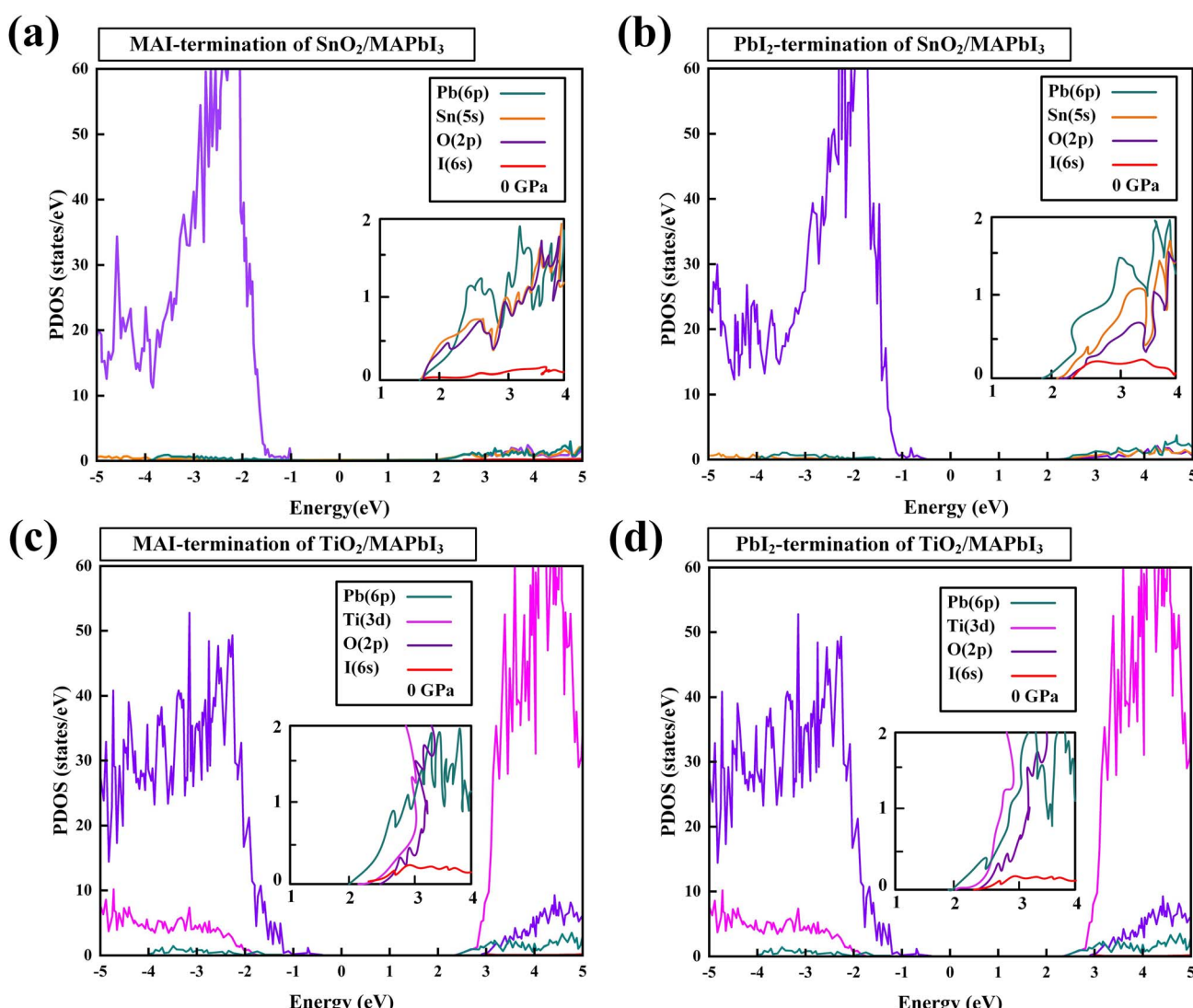


Fig. 3 PDOS of $\text{SnO}_2/\text{MAPbI}_3$ heterojunction interface: (a) MAI-termination and (b) PbI_2 -termination. $\text{TiO}_2/\text{MAPbI}_3$ heterojunction interface: (c) MAI-termination and (d) PbI_2 -termination. [Sn-5s orbital (orange), Ti-3d orbital (pink), O-2p orbital (purple), Pb-6p orbital (turquoise), and I-6s orbital (red)].



composed of the valence electrons of Pb atoms. Similarly, the VBM (Valence Band Maximum) at the left side of the Fermi level, that is, the valence band top of TiO_2 , is mainly composed of the valence electrons of O atoms, and the VBM at the valence band top of MAPbI_3 is mainly composed of the valence electrons of I. The electronic DOS of MA atomic groups is far away from the Fermi level, and there are no peaks near the VBM and the CBM.^{32,33} Most of the electron transport exists between the Pb-I framework and TiO_2 , and MA atomic groups basically do not participate in the electron transport between the interfaces.³⁴⁻³⁶ Ti forms a chemical bond with I in MAPbI_3 , and electrons are transported from the surface of MAPbI_3 to TiO_2 .³⁷⁻⁴⁰ The Fermi energy level is at the top of the valence band, and the right side of the Fermi energy level, which is the bottom CBM of SnO_2 , is basically composed of the valence electrons of Sn atoms, while the bottom CBM of MAPbI_3 is mainly the valence electrons of Pb atoms, as shown in Fig. 2(a)-(c). Similarly, the VBM of SnO_2 on the left side of the Fermi energy level is mainly composed of the valence electrons of O atoms, and the VBM of MAPbI_3 is mainly composed of the valence electrons of I. It is also analyzed that the electronic density of states of the MA atomic group is far away from the Fermi level, and there is no wave peak near the top of the VBM and the bottom of the CBM. Therefore, most of the electron transfer exists between the Pb-I skeleton and SnO_2 , and the MA atomic group does not participate in the charge transfer between interfaces. Through the formation of a chemical bond between Sn and I in MAPbI_3 , electrons are transferred from the MAPbI_3 surface to the SnO_2 surface. On the surface of Pb-I, the force of interface atoms is Pb-O atomic force. On the

right side of the Fermi energy level is the bottom CBM of TiO_2 which is basically composed of valence electrons of Ti atoms, and the bottom CBM of MAPbI_3 is mainly composed of valence electrons of Pb atoms, as shown in Fig. 2(d)-(f). Similarly, the top VBM of TiO_2 on the left side of the Fermi energy level is mainly composed of the valence electrons of O atoms, and the top VBM of MAPbI_3 is mainly composed of the valence electrons of I. The electronic state density of the MA atomic group is far away from the Fermi energy level, and there is no wave peak near the top VBM and the bottom CBM. Therefore, most of the electron transfer exists between the Pb-I skeleton and TiO_2 . The MA atomic group does not participate in the charge transfer between interfaces. The electron transfers from the MAPbI_3 surface to the TiO_2 surface through the chemical bond formed between O and Pb in MAPbI_3 . The charge transport driving force of $\text{TiO}_2/\text{MAPbI}_3$ heterostructure interfaces $E_d(\text{TiO}_2/\text{MAPbI}_3)$ is:

$$\Delta E_d(\text{TiO}_2/\text{MAPbI}_3) = \text{CBM}(\text{MAPbI}_3) - \text{CBM}(\text{TiO}_2) \quad (3)$$

On the Pb-I surface, the atomic force is displayed at the interface. The Fermi level is set at position 0, and the width of the band gap is about 0.45 eV.

For the $\text{SnO}_2/\text{MAPbI}_3$ heterojunction interface, the bottom CBM of the conduction band of SnO_2 is basically composed of the valence electrons of Sn atoms, and the bottom CBM of MAPbI_3 is mainly the valence electrons of Pb atoms.^{41,42} The electronic DOS of the MA atomic group is also far away from the Fermi level, and no peak is observed near the VBM and CBM. Most of the electron transport exists between the Pb-I skeleton

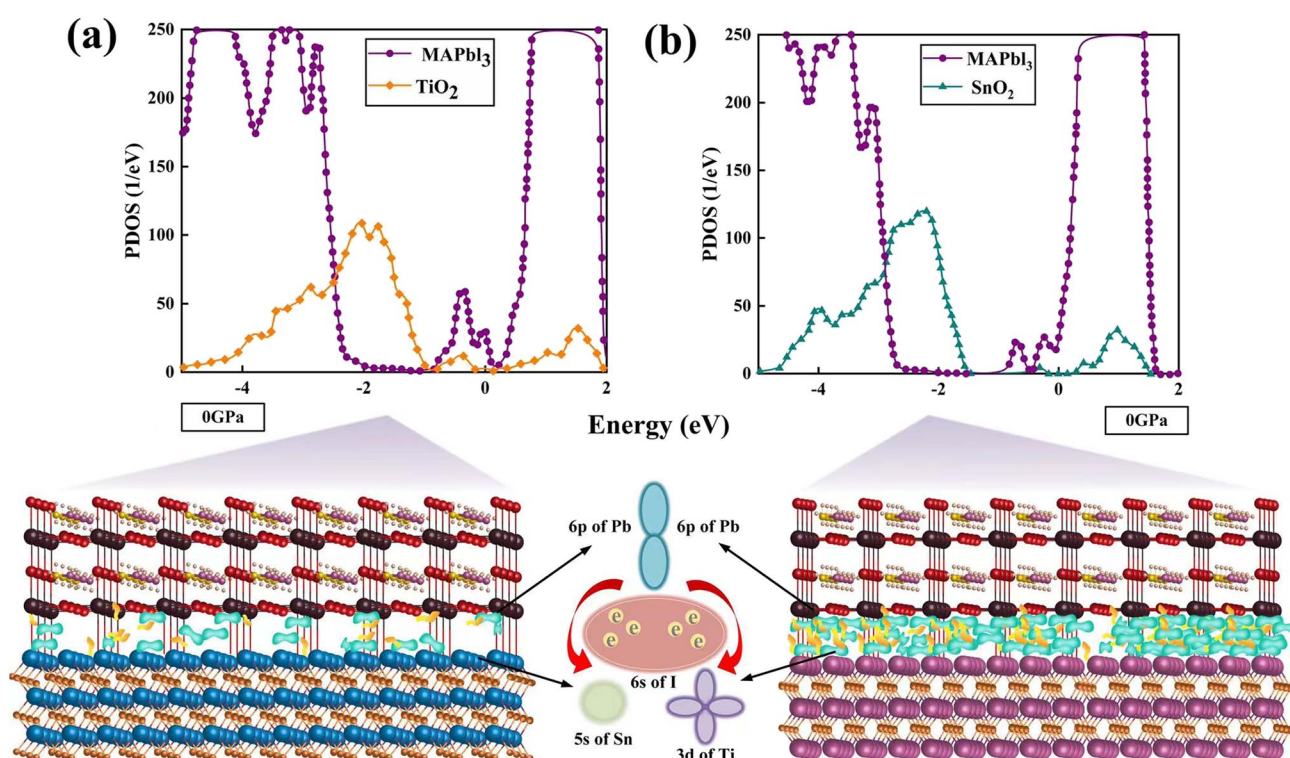


Fig. 4 PDOS of interface layer and differential charge density (a) on $\text{TiO}_2/\text{MAPbI}_3$, (b) on $\text{SnO}_2/\text{MAPbI}_3$ under ambient conditions. The yellow area represents gaining electrons, and the green area represents losing electrons.



and SnO_2 , and the MA atomic group basically does not participate in the electron transport between heterostructure interfaces. Electrons are transported from the surface of MAPbI_3 to the surface of SnO_2 through the formation of a chemical bond between O and Pb in MAPbI_3 .⁴³ The charge transport driving force of $\text{SnO}_2/\text{MAPbI}_3$ heterojunction interfaces $E_d(\text{SnO}_2/\text{MAPbI}_3)$ is:

$$\Delta E_d(\text{SnO}_2/\text{MAPbI}_3) = \text{CBM}(\text{MAPbI}_3) - \text{CBM}(\text{SnO}_2) \quad (4)$$

$\Delta E_d(\text{SnO}_2/\text{MAPbI}_3)$ is around 1.45 eV, while $\Delta E_d(\text{TiO}_2/\text{MAPbI}_3)$ is about 0.75 eV. Since $1.45 \text{ eV} > 0.75 \text{ eV}$, the $\text{SnO}_2/\text{MAPbI}_3$ heterojunction interface has stronger charge transfer driving ability, showing superior electrical transport properties under ambient conditions. In order to study the electrical transport properties of $\text{SnO}_2(\text{TiO}_2)/\text{MAPbI}_3$ heterojunction interfaces under compression conditions, $E_d(\text{SnO}_2(\text{TiO}_2)/\text{MAPbI}_3)$ and $\Delta E_d(\text{SnO}_2(\text{TiO}_2)/\text{MAPbI}_3)$ are obtained from ambient pressure to 20 GPa (Table S6 in the ESI[†]). It can be clearly seen that with the

increase in the applied pressure to 20 GPa, the larger ΔE_d between the charge transfer driving forces of $\text{SnO}_2/\text{MAPbI}_3$ and $\text{TiO}_2/\text{MAPbI}_3$ heterojunction interfaces reflects a more obvious difference in electrical transport properties. Note that the $\text{SnO}_2/\text{MAPbI}_3$ heterojunction interface shows a greater pressure dependence for the electrical transport properties than the $\text{TiO}_2/\text{MAPbI}_3$ heterojunction interface.

The PDOS of $\text{SnO}_2/\text{MAPbI}_3$ and $\text{TiO}_2/\text{MAPbI}_3$ heterojunction interfaces in MAI-termination and PbI_2 -termination are shown in Fig. 3(a)–(d). The CBMs of SnO_2 , TiO_2 , and MAPbI_3 are mostly composed of Sn-5s, Ti-3d, and Pb-6p, respectively. The CBM orbital hybridizations occur between Sn-5s and Pb-6p orbitals at the $\text{SnO}_2/\text{MAPbI}_3$ interface and between Ti-3d and Pb-6p at the $\text{TiO}_2/\text{MAPbI}_3$ interface. The binding energies on the MA orientations of [001], [011] and [111] of MAI-termination and PbI_2 -termination $\text{SnO}_2/\text{MAPbI}_3$ and $\text{TiO}_2/\text{MAPbI}_3$ are obtained (Tables S7–S10 in ESI[†]).

The binding energy of the PbI_2 -termination of the $\text{SnO}_2/\text{MAPbI}_3$ heterojunction interface is greater than that of MAI-

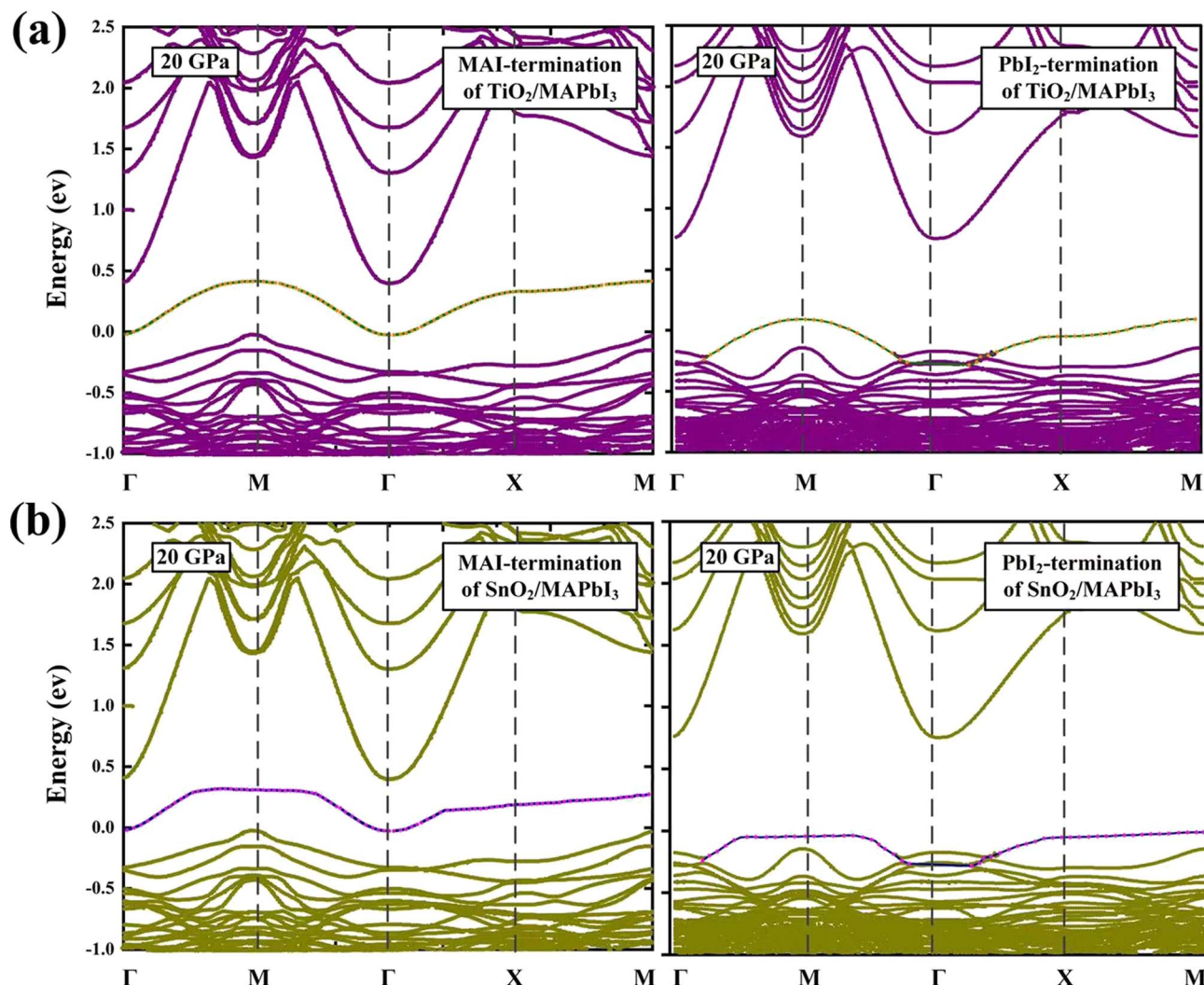


Fig. 5 Band structures of $\text{TiO}_2/\text{MAPbI}_3$ and $\text{SnO}_2/\text{MAPbI}_3$ heterojunction interfaces: (a) MAI-termination and PbI_2 -termination, (b) MAI-termination and PbI_2 -termination at 20 GPa. The pink and blue alternative circles and the orange and green alternative circles indicate the contribution of the surface Sn-5s states and Ti-5s states, respectively.



termination under different pressures, showing in the orbital hybridization of Pb (MAPbI₃) and Sn (SnO₂) interface atoms at the PbI₂-termination, which is conducive to efficient electron extraction. The orbital hybridization in the SnO₂/MAPbI₃ heterojunction interface is greater than that in TiO₂/MAPbI₃ owing to that the d orbital does not strongly hybridize with the s orbital or p orbital generally.^{44,45} We note that the orbital hybridization difference is closely related to the carrier injection performance of the SnO₂(TiO₂)/MAPbI₃ heterostructure interfaces, showing that the SnO₂/MAPbI₃ heterojunction interface has better carrier injection due to the greater orbital hybridization compared with that at the TiO₂/MAPbI₃ heterojunction interface.²¹

The DOS of the SnO₂(TiO₂)/MAPbI₃ heterojunction interfaces are calculated to verify the SnO₂/MAPbI₃ heterojunction interface effectively reduces the trap energy level compared with the TiO₂/MAPbI₃ heterojunction interface under ambient conditions, as shown in Fig. 4(a) and (b). The trap energy levels in the interface band gaps of SnO₂/MAPbI₃ and TiO₂/MAPbI₃ heterojunction interfaces are used as the carrier binding center in the process of interface charge transfer.⁴⁶ The trap density is approximately 23.4% lower than that of the TiO₂/MAPbI₃ heterojunction interface, attributed to the trap energy level only existing in SnO₂ for the SnO₂/MAPbI₃ heterojunction interface. The SnO₂/MAPbI₃ heterojunction interface effectively reduces the defects affecting interface charge transfer and the trap energy level to reduce carrier recombination, which almost eliminates the interface defects caused by interface action in perovskites. The electron-capture rate of the TiO₂/MAPbI₃ heterojunction interface is approximately 27.5% more than that of SnO₂/MAPbI₃. Compared with the TiO₂/MAPbI₃ heterojunction interface, the SnO₂/MAPbI₃ heterostructure interface is less prone to capture electrons.

The band structures of the TiO₂/MAPbI₃ and SnO₂/MAPbI₃ heterojunction interfaces with Vo₀ are shown in Fig. 5(a) and (b) at 20 GPa. Corresponding to the PDOS of Fig. 4(a) and (b), the zero of energy represents the top of the valence band for the MAI-termination and PbI₂-termination of the TiO₂/MAPbI₃ and SnO₂/MAPbI₃ heterojunction interfaces. The green and orange alternative circles indicate the contribution of the surface Ti-5s states. The surface becomes a TiO-like environment attributed to the Vo₀ which makes the Ti-5s state almost filled with electrons.⁴⁷ For the MAI-termination and PbI₂-termination of SnO₂/MAPbI₃, the contribution of the surface Sn-5s states is shown by the pink and blue alternative circles. The surface becomes a SnO-like environment due to the Vo₀ filling the Sn-5s state with electrons. The SnO-like environment has better electron filling density, showing a superior electron transport environment compared with the TiO-like environment. The electron concentration difference in the SnO-like environment will be greater, which will result in greater electron transport ability compared with the TiO-like environment.

4. Conclusions

The SnO₂/MAPbI₃ heterojunction interface shows superior electrical transport properties compared with the TiO₂/MAPbI₃

heterostructure interface up to 20 GPa, manifested in the density of trap energy levels, binding energy, charge transfer driving force and defects, and charge-capture rate. The trap energy level of SnO₂/MAPbI₃ only exists in SnO₂, and the density of the trap energy level (23.4%) is much lower. The charge transfer driving force of the SnO₂/MAPbI₃ heterojunction interface (1.45 eV) is greater than that of TiO₂/MAPbI₃ (0.75 eV). The binding energy (-1.02 eV nm^{-2}) of the SnO₂/MAPbI₃ heterojunction interface is significantly higher than that of TiO₂/MAPbI₃ (-6.75 eV nm^{-2}), showing the obviously more stable SnO₂-based heterojunction structure. The electron-capture rate of the TiO₂/MAPbI₃ heterojunction interface is approximately 27.5% more than that of SnO₂/MAPbI₃. Compared with the TiO₂/MAPbI₃ heterojunction interface, the SnO₂/MAPbI₃ heterostructure interface is less prone to capture electrons, which is shown by the greater electron concentration difference in the SnO-like environment attributed to Vo₀ compared with the TiO-like environment.

Conflicts of interest

There are no conflicts to declare.

Acknowledgements

This work was supported by the National Natural Science Foundation of China (Grant Nos. 11804249, 61804107), and the Natural Science Foundation of Tianjin City (Grant Nos. 18JCQNJC03700, 18JCYBJC85400, 20JCQNJC00180).

References

- 1 B. O'Regan and M. Grätzel, *Nature*, 1991, **353**, 737–740.
- 2 A. L. Linsebigler, G. Lu and J. T. Yates, *Chem. Rev.*, 1995, **95**, 735–758.
- 3 U. Bach, D. Lupo, P. Comte, J. E. Moser, F. Weissortel, J. Salbeck, H. Spreitzer and M. Grätzel, *Nature*, 1998, **395**, 583–585.
- 4 E. Mosconi, E. Ronca and F. D. Angelis, *J. Phys. Chem. Lett.*, 2014, **5**, 2619–2625.
- 5 J. Jeng, Y. Chiang, M. Lee, S. Peng, T. Guo, P. Chen and T. Wen, *Adv. Mater.*, 2013, **25**, 3727–3732.
- 6 J. H. Heo, S. H. Im, J. H. Noh, T. N. Mandal, C. S. Lim, J. A. Chang, Y. H. Lee, H. J. Kim, A. Sarkar, M. K. Nazeeruddin, M. Grätzel and S. I. Seok, *Nat. Photonics*, 2013, **7**, 486–491.
- 7 J. Haruyama, K. Sodeyama, I. Hamada, L. Han and Y. Tateyama, *J. Phys. Chem. Lett.*, 2017, **8**, 5840–5847.
- 8 K. C. Ko, S. T. Bromley, J. Y. Lee and F. Illas, *J. Phys. Chem. Lett.*, 2017, **8**, 5593–5598.
- 9 J. Jeon, T. Eom, E. Lee, S. Kim, S. Kim, K.-H. Hong and H. Kim, *J. Phys. Chem. C*, 2017, **121**, 9508–9515.
- 10 C. Motta, F. E. Mellouhi, S. Kais, N. Tabet, F. Alharbi and S. Sanvito, *Nat. Commun.*, 2015, **6**, 7026.
- 11 F. Zheng, L. Z. Tan, S. Liu and A. M. Rappe, *Nano Lett.*, 2015, **15**, 7794–7800.





12 C. W. Myung, S. Javaid, K. S. Kim and G. Lee, *ACS Energy Lett.*, 2018, **3**, 1294–1300.

13 F. D. Angelis, D. Meggiolaro, E. Mosconi, A. Petrozza, M. K. Nazeeruddin and H. J. Snaith, *ACS Energy Lett.*, 2017, **2**, 857–861.

14 K. Oh, K. Jung, J. Shin, S. Ko and M.-J. Lee, *J. Mater. Sci. Technol.*, 2021, **92**, 171–177.

15 T. Leijtens, G. E. Eperon, S. Pathak, A. Abate, M. M. Lee and H. J. Snaith, *Nat. Commun.*, 2013, **4**, 2885.

16 D. Yang, X. Zhou, R. Yang, Z. Yang, W. Yu, X. Wang, C. Li, S. F. Liu and R. Chang, *Energy Environ. Sci.*, 2016, **9**, 3071–3078.

17 S. S. Shin, E. J. Yeom, W. S. Yang, S. Hur, M. G. Kim, J. Im, J. Seo, J. H. Noh and S. I. Seok, *Science*, 2017, **356**, 167–171.

18 F. Giordano, A. Abate, J. P. C. Baena, M. Saliba, T. Matsui, S. H. Im, S. M. Zakeeruddin, M. K. Nazeeruddin, A. Hagfeldt and M. Graetzel, *Nat. Commun.*, 2016, **7**, 10379.

19 X. Guo, J. Du, Z. Lin, J. Su, L. Feng, J. Zhang, Y. Hao and J. Chang, *Chem. Eng. J.*, 2021, **407**, 127997.

20 B. Park, *Results Phys.*, 2021, **23**, 104025.

21 J. Kim, K. S. Kim and C. W. Myung, *npj Comput. Mater.*, 2020, **6**, 100.

22 Y. Chen, Y. He, J. Wang, M. Li, M. Yu, R. Ye, B. Geng, Z. Yang, X. Zeng and J. Hu, *J. Phys. Chem. Lett.*, 2021, **12**, 989–996.

23 Y. Li, J. K. Cooper, R. Buonsanti, C. Giannini, Y. Liu, F. M. Toma and I. D. Sharp, *J. Phys. Chem. Lett.*, 2015, **6**, 493–499.

24 J. P. Perdew, K. Burke and M. Ernzerhof, *Phys. Rev. Lett.*, 1996, **77**, 3865.

25 A. Tkatchenko and M. Scheffler, *Phys. Rev. Lett.*, 2009, **102**, 073005.

26 G. Kresse and J. Furthmuller, *Comput. Mater. Sci.*, 1996, **6**, 15.

27 Y. Guo, Y. Xue and L. Xu, *Comput. Mater. Sci.*, 2021, **187**, 110081.

28 L. Wang, F. Si, F. Tang and H. Xue, *Mater. Res. Express*, 2019, **6**, 026312.

29 R. A. Kerner and B. P. Rand, *J. Phys. Chem. Lett.*, 2017, **8**, 2298–2303.

30 S. Ito, S. Tanaka and H. Nishino, *J. Phys. Chem. Lett.*, 2015, **6**, 881–886.

31 F. Zheng, L. Z. Tan, S. Liu and A. M. Rappe, *Nano Lett.*, 2015, **15**, 7794–7800.

32 F. Zhang, S. Y. Park, C. Yao, H. Lu, S. P. Dunfield, C. Xiao, S. Uličná, X. Zhao, L. D. Hill, X. Chen, X. Wang, L. E. Mundt, K. H. Stone, L. T. Schelhas, G. Teeter, S. Parkin, E. L. Ratcliff, Y.-L. Loo, J. J. Berry, M. C. Beard, Y. Yan, B. W. Larson and K. Zhu, *Science*, 2022, **375**, 71–76.

33 D. Liu and T. L. Kelly, *Nat. Photonics*, 2014, **8**, 133–138.

34 S. Zhang, J. Su, J. Zhang, Z. Lin, H. Yuan, J. Chang and Y. Hao, *J. Phys. Chem. Lett.*, 2021, **12**, 11834–11842.

35 E. P. Mukhokosi and M. Maaza, *J. Mater. Sci.*, 2022, **57**, 1555–1580.

36 J. M. Azpiroz, E. Mosconi, J. Bisquert and F. D. Angelis, *Energy Environ. Sci.*, 2015, **8**, 2118.

37 W. Shi and H. Ye, *J. Phys. Chem. Lett.*, 2021, **12**, 4052–4058.

38 K. Yan, Z. Wei, T. Zhang, X. Zheng, M. Long, Z. Chen, W. Xie, T. Zhang, Y. Zhao and J. Xu, *Adv. Funct. Mater.*, 2016, **26**, 8545–8554.

39 J. Zhang, K. Wang, Q. Yao, Y. Yuan, J. Ding, W. Zhang, H. Sun, C. Shang, C. Li, T. Zhou and S. Pang, *ACS Appl. Mater. Interfaces*, 2021, **13**, 29827–29834.

40 C. Yang, P. Du, Z. Dai, H. Li, X. Yang and Q. Chen, *ACS Appl. Mater. Interfaces*, 2019, **11**, 14044–14050.

41 T. Liu, L. Liu, M. Hu, Y. Yang, L. Zhang, A. Mei and H. Han, *J. Power Sources*, 2015, **293**, 533–538.

42 J. Yan, Z. Lin, Q. Cai, X. Wen and C. Mu, Choline chloride-modified SnO_2 achieving high output voltage in MAPbI_3 perovskite solar cells, *ACS Appl. Energy Mater.*, 2020, **3**, 3504–3511.

43 J. H. Heo and S. H. Im, *Nanoscale*, 2016, **8**, 2554–2560.

44 C. Li, J. Hu, S. Wang, J. Ren, B. Chen, T. Pan, X. Niu and F. Hao, *J. Phys. Chem. Lett.*, 2021, **12**, 4569–4575.

45 Y. Ai, Y. Zhang, J. Song, T. Kong, Y. Li, H. Xie and D. Bi, *J. Phys. Chem. Lett.*, 2021, **12**, 10567–10573.

46 G. S. H. Thien, N. A. Talika, B. K. Yap, H. Nakajima, S. Tunmee, N. Chanlek and B. T. Goh, *Ceram. Int.*, 2020, **46**, 29041–29051.

47 T. Bu, J. Li, F. Zheng, W. Chen, X. Wen, Z. Ku, Y. Peng, J. Zhong, Y. Cheng and F. Huang, *Nat. Commun.*, 2018, **9**, 4609.